actuators

MDPI

Article

Experimental Study on the Working Characteristics of a Methane Combustion-Driven Plasma Actuator

Hai Chen *, Hongyan Zuo, Guohai Jia and Jianyun Zheng

College of Mechanical Engineering, Hunan Institute of Engineering, Xiangtan 411104, China; zuohongyan18@126.com (H.Z.); jiaguohai@hnie.edu.cn (G.J.); 24069@hnie.edu.cn (J.Z.)
* Correspondence: chfair@163.com; Tel.: +86-0731-58688686 (ext. 411104)

Abstract

Active flow control actuators are critical for improving aerodynamic performance in applications such as aircraft lift enhancement, drag reduction, and maneuverability improvement. However, the plasma synthesis jet actuator (PSJA) is limited by the constraints of electric energy deposition, making it difficult to further improve the jet velocity and mass flow rate. Meanwhile, the jet velocity driven by combustion needs to be further increased. This study preliminarily investigated the characteristics of a combustion-driven SparkJet actuator through experiments; a combustion-driven SparkJet actuator integrates the advantages of plasma actuators and combustion-driven actuators. The actuator employs a continuous methane–air mixture supply ignited by spark discharge. High-speed shadowgraph imaging is used to characterize the jet flow field evolution. The effects of the cavity volume, normalized outlet diameter ($d^* = d/h$), and equivalence ratio on jet performance are systematically examined. As the normalized outlet diameter increases from 0.666 to 1, the jet penetration distance and jet width increase with an increasing normalized outlet diameter, owing to the reduced boundary layer blockage effect at the orifice. However, when the normalized outlet diameter equals 1, both the jet penetration distance and jet width first increase and then decrease with increasing cavity volume; hence, the outlet diameter and cavity have an optimal size. At an equivalence ratio of mixture ≤ 1, increasing the methane flow rate enhances the volumetric chemical heat release rate, thereby monotonically improving the jet width and penetration distance. The combustion-driven actuator demonstrates a significantly higher jet velocity compared to a conventional plasma actuator under identical geometric parameters; the combustion reaction can effectively amplify the jet energy and velocity of the actuator. Moreover, the combustion-driven SparkJet actuator also has the same working frequency when the actuator volume is the same, indicating that the combustion process does not significantly extend the cycle time. The maximum jet velocity first increases and then decreases with increasing cavity volume; the reason that the maximum jet velocity first increases is that a larger volume results in a greater mixture mass and more released heat; it then decreases due to incomplete combustion occurring in large chambers. These results show that the design standards for the combustion-driven actuator are fundamentally different from those for the plasma actuator, and their optimal performance is related to not only electrical energy density but also combustion performance. The design parameters of the combustion-driven actuator can be optimized to maximize the jet front velocity. The experimental data in this article provides a reference for optimizing the performance of combustion-driven actuators.

Keywords: actuator; combustion-driven actuator; SparkJet; plasma actuator

Check for updates

Academic Editor: Pedro Javier Gamez-Montero

Received: 12 June 2026
Revised: 20 July 2026
Accepted: 3 August 2026
Published: 11 August 2026

Copyright: © 2026 by the authors. Licensee MDPI, Basel, Switzerland. This article is an open access article distributed under the terms and conditions of the Creative Commons Attribution (CC BY) license.

1. Introduction

Actuation technologies for flow control have been studied extensively [1–4]. The effective control of flow fields can improve aerodynamic characteristics such as range, payload, and maneuverability. Commonly used actuators include fluidic, mechanical, and plasma devices [5]. Fluidic actuators consist of pulsed jet and combustion-driven SparkJet actuators, while plasma actuators include spark discharge, DC, and dielectric-barrier discharge types. Owing to their robustness, simple structure, sufficient bandwidth, and fast response, these actuators can improve the aerodynamic characteristics of aircraft, making them a new hotspot in research.

The Johns Hopkins University Applied Physics Laboratory first proposed the SparkJet actuator in 2003 [6]. Experiments and numerical simulations demonstrated that the actuator can generate high-speed jets. The SparkJet actuator consists of a cavity, two electrodes, and a lid with an orifice (Figure 1). Narayanaswamy V. et al. [7] carried out experiments on the performance characteristics of a pulsed-plasma jet actuator and found that it has high-speed jet ejection and great application prospects in active flow control. Huang H.X. et al. [8] employed high-speed Schlieren imaging to research the rapid flow evolution induced by the interaction between a 20° compression ramp flow and a plasma jet at Mach 2.0. Li J.F. and Zhang X.B. et al. [9] designed a new actuator by replacing the bottom of a plasma synthetic jet actuator (PSJA) with a piezoelectric-driven diaphragm. Their numerical results indicated that the new actuator has higher gas-refilling rates and peak velocity of the synthetic jet compared with the SparkJet actuator. Liu R.B. and Lin Q. et al. [10] proposed a new PSJA with an air-supplementing structure that can raise the maximum jet flow speed by nearly 20%. The research team at Air Force Engineering University [11–13] examined the discharge parameters, structural parameters, and other parameters of actuators using particle image velocimetry (PIV) shadowgraphs and numerical simulation. Kim et al. [14] numerically investigated the performance of a SparkJet actuator and studied pressure waves in the chamber in relation to actuator performance. Zheng B. et al. [15] proposed a self-supplementing dual-cavity PSJA and experimentally and numerically investigated its static properties. The new actuator improves jet flow intensity at high frequencies and reduces refresh time by supplementing air to the top chamber through a hole. Wu et al. [16] investigated the effects of the pulse rise time, amplitude, and repetition frequency of the pulse voltage on the jet flow. Zhang et al. [17] numerically investigated the internal characteristics of the PSJA and found that the base frequencies are inversely proportional to the chamber height and width, while the peak jet velocity rises along with the chamber width or height.

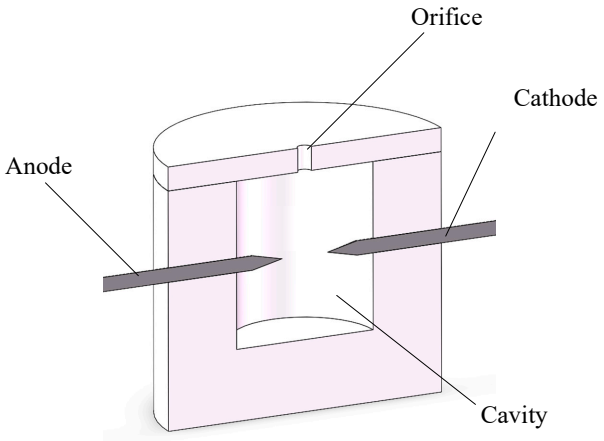


Figure 1. Two-electrode plasma synthetic jet actuator.

Zong et al. [18] experimentally investigated the effect of the outlet aperture shape on the operating performance of a three-electrode PSJA. They found a strong correlation between the shapes of the outlet aperture and the starting vortex ring. When the outlet area remained the same, the aperture shape had little effect on the outlet velocity. Yue L. et al. [19] numerically studied the airflow field under different inflow velocity power frequencies and loading voltages. The results indicated that the induced velocity rises linearly with power frequency, while the working range of the actuator in the vertical direction remains unchanged. Nguyen H.H. et al. [20] carried out a single 50 mJ spark pulse experiment and found that the Joule heating factor accounts for approximately 5% of the heat source term. Additionally, the SparkJet actuator has higher efficiency because a double spark pulse has a sufficient time delay. To improve the jet performance and gas-supplying ability, Liu R. et al. [21] designed an air-supplied actuator with a valve connected to the chamber. The results showed that the gas pressure in the chamber is closer to the initial discharge state and that the suction airflow velocity is doubled. Cheng L. et al. [22] compared the flow field characteristics of PSJAs with slots and hole-shaped outlets through a numerical study and found that slot-type PSJAs have better planar characteristics and flow control uniformity. Zhang X. et al. [23] experimentally studied an opposing plasma synthetic jet in a Mach 8 wind tunnel and observed that drag was reduced by an average of 13.25% and maximum drag by 40.27% in one discharge cycle. Moreover, the average drag reduction improved as the nozzle diameter increased, while the effective control duration dropped. Liu R. et al. [24] used programmable high-voltage pulses and a Marx high-voltage generator to trigger and regulate the discharge frequency of the PSJA array, achieving the highest jet speed of 70 m/s. Shin J.Y. et al. [25] investigated the effects of the energy deposition amount and electrode position on the operating characteristics of SparkJet actuators. They also proposed a new variable that can predict pulse trends related to the electrode position. Kong Y. et al. [26] experimentally investigated the timing of flow responses to control via planar PIV and high-speed schlieren imaging and found that the high-level velocity fluctuation area improves by 30%, while the growth rate of the shear layer thickness rises by nearly 10% compared with the condition without actuators. However, due to the energy injection of plasma actuators being limited by the energy density stored in the power supply, their jet momentum is relatively low.

To achieve higher momentum output, researchers have proposed combustion-driven actuators based on small-scale combustion theory [27–30], and Crittenden [31] proposed a new actuator powered by chemical energy (Figure 2). In this device, a gaseous fuel and oxidizer flow into the chamber and are ignited by a spark or another ignition source. The proposed actuator produces high-speed and high-pressure jets. The cycle repeats when a fresh mixture enters the chamber and replaces the remaining gaseous fluid. Jee S. et al. [32] experimentally and numerically investigated a combustion-driven actuator and discovered its high aerodynamic lift performance, although its jet flow velocity needs further improvement. Srinivasan [33], Rajendar [34], and Crittenden [35] experimentally and numerically investigated the influence of parameters such as the chamber volume, fuel type, chamber surface area, and mixture ratio on small-scale combustion performance.

However, the jet velocity of the combustion-driven actuators needs to be further improved. To achieve higher momentum output, researchers have proposed combustion-driven SparkJet actuators. Chen et al. [36,37] designed a new actuator that integrates a PSJA and a combustion-driven actuator. Numerical results indicated that the combustion-driven plasma actuator has a higher mass flow rate and jet velocity than the PSJA, but nearly the same saturation work frequency. Moreover, a Laval outlet structure was designed for the actuator, and the Laval outlet configuration was found to improve actuator performance. By integrating the advantages of combustion-driven actuators and PSJAs, this actuator

improves the mass flow rate, jet flow velocity, and environmental adaptability. However, the jet velocity of the combustion-driven actuators needs to be further improved.

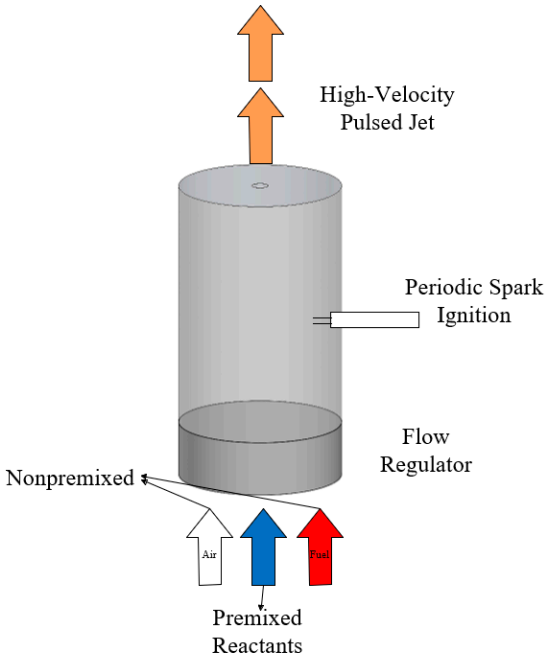


Figure 2. Schematic diagram of a combustion-driven actuator.

To date, only numerical studies have been conducted on combustion-driven plasma actuators; there has been no comprehensive experimental research on their working performance. Studies on their basic properties are still needed to achieve practical applications in active flow control. Flow field visualization, which focuses on studying the formation, development, and evolution of plasma jets, is a key method for conducting fundamental research on plasma jets and their operating mechanisms [37–43]. The present study employs high-speed shadowgraphy to measure the flow field of combustion-driven plasma jets and investigate their flow field and work characteristics.

The remainder of this paper is organized as follows. In Section 2, the experimental system setup and the parameters of the experimental equipment are described; moreover, the structure of the combustion-driven SparkJet actuators and the experimental parameters are introduced. Section 3 introduces the experimental results for the actuator under different structural parameters, gas flow rates, and equivalence ratios. Then, Section 4 presents the conclusion drawn through the above research and analysis.

2. Experimental Setup

2.1. Gas Supply System

The experimental system device (Figure 3) mainly consists of a combustion-driven SparkJet actuator, high-speed shadowgraph system, methane gas source, air compressor, flowmeter, and high-voltage pulse power supply. Methane and air are supplied by high-pressure gas cylinders and oil-free air compressors, respectively, and their flow rates are regulated by mass flowmeters before they enter the actuator. Methane and air enter the actuator cavity through the bottom inlet, are mixed in the chamber, and are ignited by electrode discharge. The energy released by combustion rapidly pressurizes the cavity, causing high-temperature combustion products to be ejected from the orifice. In this study, the air flow rate was fixed at 800 mL/min, while the methane flow rate was varied from 21 to 84 mL/min, corresponding to an equivalence ratio range of $\varphi = 0.25$ to 1.

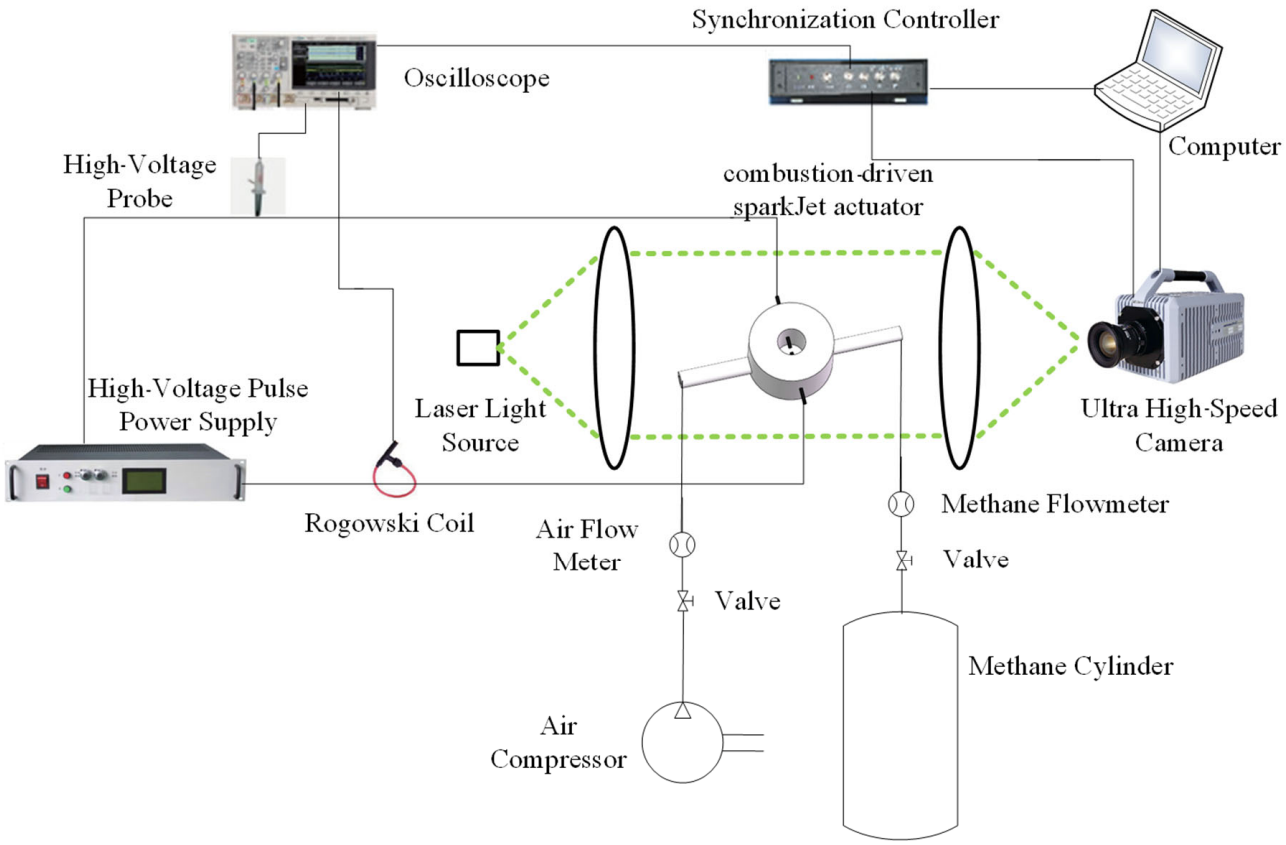


Figure 3. Experimental setup for combustion-driven SparkJet actuator.

2.2. Power Supply System

A KD-1 high-voltage pulse power supply developed by the High Voltage Laboratory of Xi'an Jiaotong University was used as the excitation source (Figure 4a). The maximum output energy of a single pulse is approximately 20 J, with a pulse frequency adjustable from 1 Hz to 50 Hz. The maximum output voltage is 10 kV. In addition, the high-voltage pulse power supply requires an external voltage regulator. This experiment used a TSGC2-15KVA three-phase contact voltage regulator (Figure 4b), with an input voltage of 380 V and an output voltage adjustable from 0 to 430 V.



(**a**) High-voltage pulse capacitive power supply(**b**) voltage regulator

Figure 4. Power supply.

2.3. Measurement System

2.3.1. Discharge Waveforms

The voltage during discharge was measured using a Tecktronic P6015A high-voltage probe and collected with a Tecktronic DPO3014 digital oscilloscope (Tektronix, Inc., Beaverton, OR, USA). The performance indicators of the above electrical parameter-measuring instruments are shown in Table 1.

Table 1. Performance indicators for electrical parameter-measuring instruments.

Tek P6015A High-Voltage Probe	Maximum root mean square voltage: 20 kV Maximum pulse (pulse width: 100 ms) voltage: 40 kV DC bandwidth: 75 MHz Attenuation factor: 1000 Rise time: 4 ns Load: 100 M Ω/3 pF
Tek DPO3014 oscilloscope	Simulated bandwidth of 100 MHz Maximum analog sampling rate of 2.5 Gs/s 4 channels Record length (memory) of 20 M
AT826 LCR digital bridge	Measurement accuracy: 0.2% The acquisition frequency is adjustable at 100 Hz, 1 kHz, and 10 kHz Inductance measurement range: 0.01 μH~9999 H Capacitance measurement range: 0.01 pF~9999 F Resistance measurement range: 0.0001 Ω~99.99 MΩ Output impedance: 100 Ω

2.3.2. High-Speed Photography and Shadowgraphy

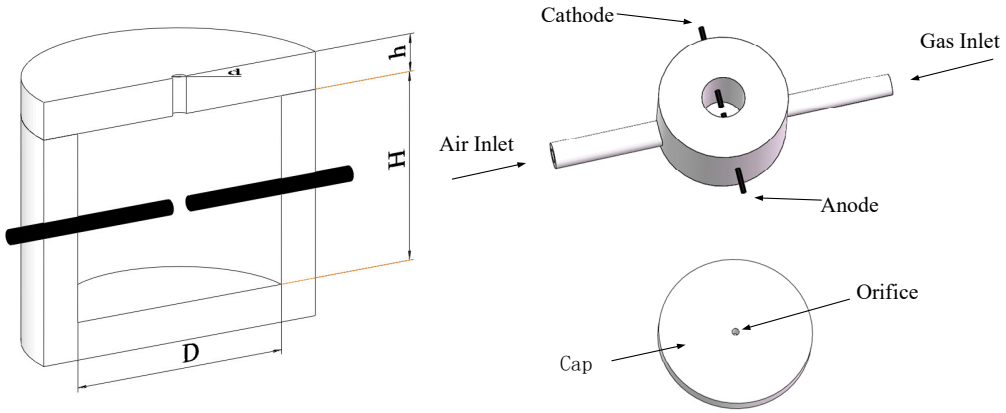
The high-speed schlieren system included two concave lenses with a diameter of 20 cm, a continuous-wave laser light source with a wavelength of 532 nm, and an ultra-high-speed camera. The flow field sampling and discharge triggering were synchronized using a synchronous controller (Micro Pulse 725).

2.4. Combustion-Driven SparkJet Actuator

The structure of the combustion-driven SparkJet actuator (Figure 5) consists of three parts: a cover with outlet holes, a discharge electrode, and an actuator chamber. During the experiment, methane and air were introduced into the chamber through separate gas and air inlets and then ignited by discharge. The chamber and cover were made from HP nylon and fiberglass, respectively. The electrode was a tungsten needle with a diameter of 1 mm, a high melting point, and resistance to electrical erosion. The factors influencing the flow field formation and development of combustion-driven plasma jets include the driving parameters, structural parameters, and working environment of the actuator.

This study investigated the effects of the jet outlet aperture, chamber height, chamber diameter, methane flow rate, and air flow rate on the flow characteristics of combustion-driven SparkJet actuator. The operating conditions are as follows: the discharge frequency of the actuator was 1 Hz, the default methane inlet flow rate was 84 mL/min, and the air inlet flow rate of the plasma jet actuator was 800 mL/min. The key geometric parameters of the actuator include the cavity diameter (D), cavity height (H), cap height (h = 3 mm), cavity volume V_c, and outlet aperture diameter (d). The spacing between the anode and cathode is 2 mm, and the inner diameters of the gas and air inlets are 10 mm. Table 2 lists

the variable parameters including the actuator cavity diameter (D), height (H), and cap outlet aperture (d).



(**a**) actuator dimensional parameters (**b**) actuator component structure

Figure 5. Actuator parameters.

Table 2. Actuator structural parameters.

Actuator Parameters	V_c/mm^3	H/mm	D/mm
	3140	10	20
	4710	15	20
	9231	15	28
	6280	20	20
	12,308	20	28
	18,840	15	40
	25,120	20	40

3. Results and Discussion

3.1. Influence of Actuator Structural Parameters

This study investigated the jet flow fields of actuators with different outlet apertures at 600 μs after discharge initiation. The outlet apertures d were 2, 2.6, and 3 mm, and the cavity volumes V_c were 3140, 4710, 9231, 6280, 12,308, 18,840, and 25,120 mm^3. Shadowgraph images are shown in Figures 6–9. To facilitate quantitative comparisons across different geometric configurations, the outlet orifice diameter d was normalized by the cap height h, yielding the normalized outlet diameter d* = d/h. As shown in the figure, when the normalized outlet diameter d* approximately equals 0.666, the combustion-driven SparkJet actuator with a volume of 3140 mm^3 produces the maximum jet penetration distance and jet width relative to the actuator outlet, and the jet penetration distance equals nearly 7.2 cm. As the actuator volume rises to 4710 mm^3, the jet penetration distance from the actuator outlet and the jet width decrease, and the jet penetration distance drops to nearly 6.4 cm. As the volume continues to increase, both the jet penetration distance and jet width drop significantly. Meanwhile, when the normalized outlet diameter d* approximately equals 0.866, both the jet penetration distance and jet width initially increase with a rise in volume and reach peak values at a volume of 4710 mm^3, where the jet penetration distance equals 7.4 cm. Further increases lead to a decreasing trend for both the jet penetration distance and width. When the normalized outlet diameter d* and V_c equal 1 and 4710 mm^3, respectively, the jet penetration distance to the actuator outlet and the jet intensity are the highest, and the jet penetration distance equals nearly 7.7 cm. The reason is that, as the volume increases from

3140 mm^3 to 4710 mm^3, the mixture mass in the chamber increases proportionally. The total heat released and the resulting peak pressure and temperature in the chamber also increase accordingly under the premise of complete combustion. As the volume further increases, the jet performance actually decreases. This is because, for methane air combustion with a chemical equivalence ratio at atmospheric pressure, the laminar flame velocity is about 0.40 m/s, which is several orders of magnitude lower than the characteristic jet velocity. As the volume of the cavity increases, the flame propagation distance becomes large. Therefore, part of the unburned mixture is discharged from the chamber, which not only reduces the chemical energy utilization rate but also lowers the average pressure of the chamber. In the plasma synthesis jet actuators, energy deposition is limited to the discharge process, and due to the fixed energy stored in the capacitor, the energy density monotonically decreases with increasing cavity volume. Therefore, the jet velocity of the plasma actuators monotonically decreases as the cavity volume increases. The design optimization of combustion-driven actuators must consider both chemical kinetics and cavity geometry, which do not need to be considered for plasma synthesis jet actuators. Therefore, combustion-driven actuators have an optimal volume parameter, and the design considerations for combustion-driven plasma actuators are different from those for plasma actuators. For actuators with the same structural parameters of the cavity, the jet penetration distance from the outlet and the jet width increase along with the normalized outlet diameter. This is because the excessively small normalized outlet diameter increases the relative thickness of the boundary layer at the outlet throat, increasing the blocking effect of the boundary layer. The results indicate that the normalized outlet diameter has an optimal value.

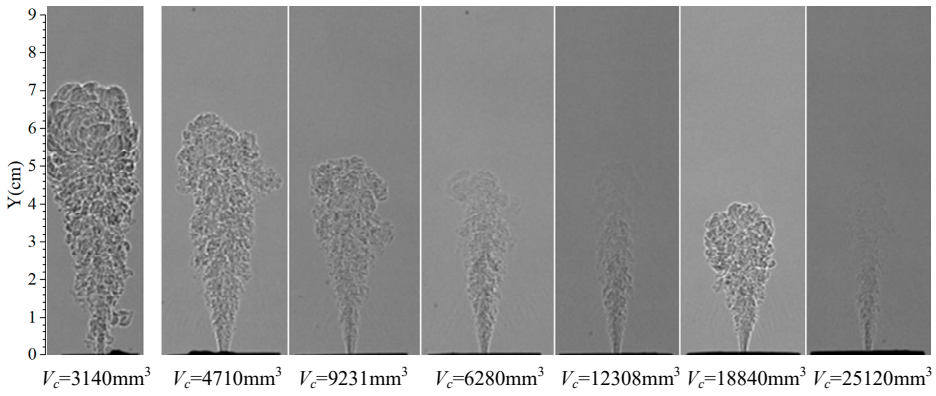


Figure 6. Shadowgraph images of combustion-driven SparkJet actuators with different cavity volumes at 600 μs after discharge initiation when d* approximately equals 0.666.

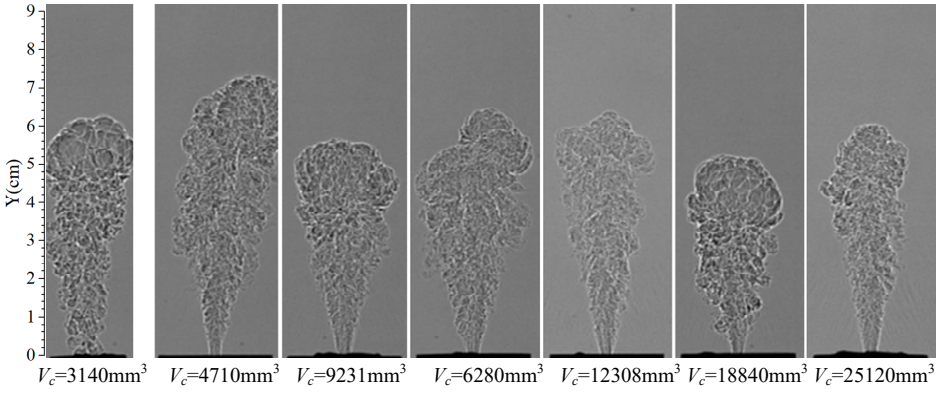


Figure 7. Shadowgraph images of combustion-driven SparkJet actuators with different cavity volumes at 600 μs after discharge initiation when d* approximately equals 0.866.

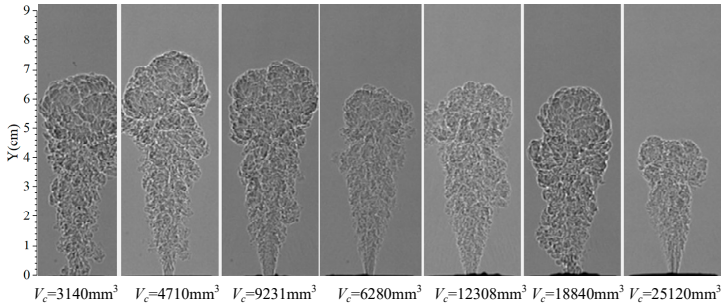


Figure 8. Shadowgraph images of combustion-driven SparkJet actuators with different cavity volumes at 600 μs after discharge initiation when d* equals 1.

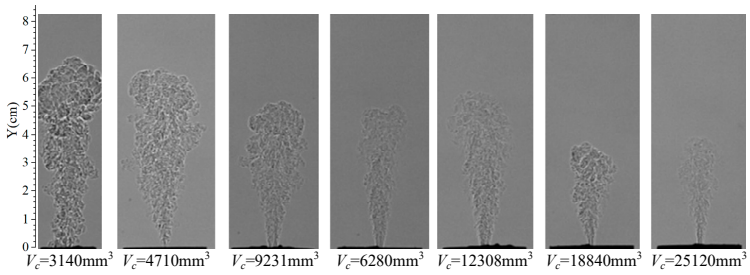


Figure 9. Shadowgraph images of PSJ actuators with different cavity volumes at 600 μs after discharge initiation when d* equals 1.

3.2. Comparison of Jet Performance Between Combustion-Driven Plasma Actuator and Plasma Actuator

3.2.1. Influence of Different Chamber Volumes and Normalized Outlet Diameter on Jet Flow Field Characteristics

The jet flow field structures of actuators with different normalized outlet diameters at 600 μs after discharge initiation are shown in Figure 10. From the figure, we can see that, when d* is 1 and V_c is 3140 mm^3, the jet penetration distance of the combustion-driven SparkJet actuator is about 3% higher than that of the plasma actuator with the same structural parameters. When the chamber volume V_c increases to 4710 mm^3, the jet penetration distance of the combustion-driven spark actuator is about 22% higher than that of the plasma actuator. As the chamber volume V_c further increases to 9231 mm^3, this difference becomes more significant because the energy deposited for the plasma actuator is limited to the electrical energy of spark discharge, which is limited by the power supply capacity. In contrast, in combustion-driven SparkJet actuators, plasma discharge not only heats the gas but also ignites the mixture and releases chemical energy. A larger volume means more mass of mixture and more released chemical energy under the premise of complete combustion. Therefore, the energy released by the combustion-driven actuator is greater than that of the plasma actuator, which leads to the gas temperature and pressure inside the combustion-driven actuator chamber being higher than those in the plasma actuator. As the chamber volume increases, the heat released by combustion also increases, resulting in an increase in the distance and width of the actuator jet. As the cavity volume V_c continues to increase to 9231 mm^3, the jet penetration distance of the combustion-driven SparkJet actuator decreases to about 7.2 cm, which is lower than that of the 4710 mm^3 combustion-driven SparkJet actuator, which is about 7.6 cm. This is because the excessively large volume of the chamber increases the complete reaction time of the mixture in the chamber, causing any unburned mixtures to discharge from the chamber, which not only reduces the chemical energy utilization rate but also lowers the average pressure of the chamber, resulting in reduced actuator performance. It can be seen that the design criteria for

combustion-driven actuators and plasma-driven actuators are different: the key parameter for plasma synthesis jet actuator design is the discharge energy density, while the coupling of chemical kinetics, discharge energy, and fluid dynamic parameters must be considered for combustion-driven SparkJet actuators.

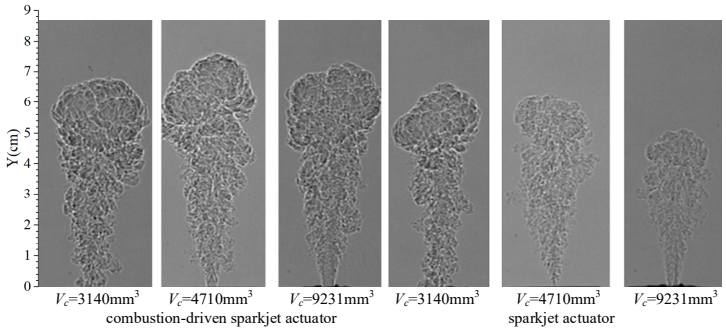


Figure 10. Shadowgraph images of actuators with different cavity volumes at 600 μs after discharge initiation with normalized outlet diameter d* of 1.

The jet flow field structure of the combustion-driven SparkJet actuator at 600 μs after discharge initiation is shown in Figure 11. The actuator has different d*, and the V_c are 3140, 4710, 6280, and 9231 mm^3. As shown in the figure, the difference between the maximum and minimum jet penetration distances of the V_c = 3140 mm^3 combustion-driven SparkJet actuator is approximately 0.8 mm. As the cavity volume rises to 4710 mm^3, the difference in jet penetration distances is approximately 1.4 mm. As the volume further increases to 6280 and 9231 mm^3, the difference in jet penetration distances rises to 1.6 mm and 2.2 mm. The influence of the normalized outlet diameter on the jet performance of the combustion-driven actuator increases with an increase in cavity volume. This is because a smaller cavity volume shortens the time for complete combustion. As a result, the pressure of the cavity rises rapidly in a short time, minimizing the impact of the boundary layer blockage.

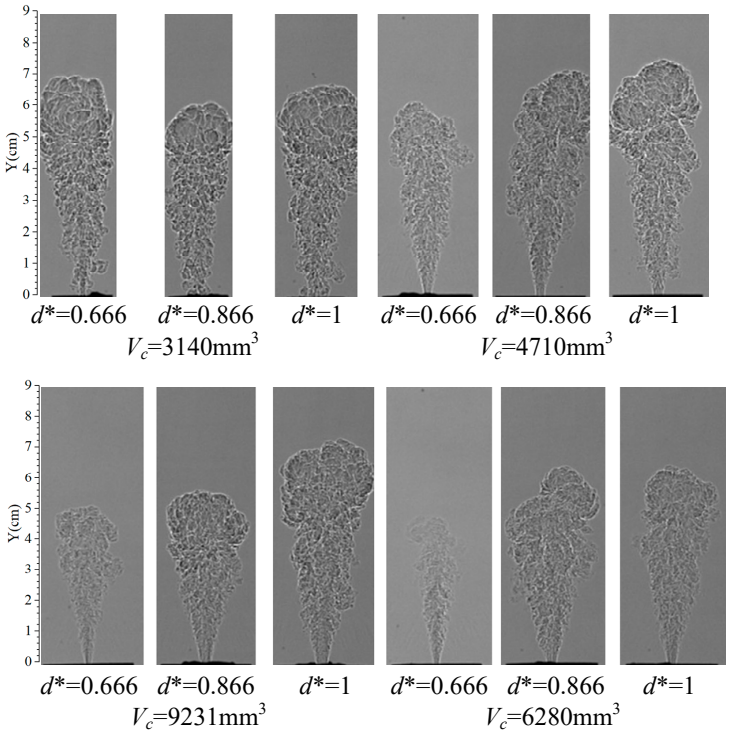


Figure 11. Shadowgraph images of the combustion-driven SparkJet actuator at different cavity volumes and normalized outlet diameter at 600 μs after the start of discharge.

3.2.2. Influence of Different Equivalence Ratios on Jet Flow Field Characteristics

Figures 12 and 13 show the jet flow field structure of the actuator at methane flow rates of 21, 42, and 84 mL/min, and an air flow rate of 800 mL/min, and the normalized outlet diameters d* are 0.866 and 1 at 600 μs after discharge initiation. The equivalence ratios equal 0.25, 0.5, and 1, respectively, and V_c are 3140 and 4710 mm^3. For the Vc = 3140 mm^3 combustion-driven SparkJet actuator, the jet penetration distance from the outlet is about 4.6 cm equivalence ratios and d* equals 0.25 and 0.866. The jet penetration distance increases as φ and d* increase, and peaks at 6.8 cm as φ and d* each separately equal 1, yielding a 48% improvement. As the cavity volume V_c of the combustion-driven SparkJet actuator increases to 4710 mm^3, the jet penetration distance from the outlet increases correspondingly. The jet penetration distance from the outlet is about 5.5 cm as the equivalence ratios and d* equals 0.25 and 0.866, and the jet penetration distance peaks at 7.5 cm when the equivalence ratios and d* both equal 1, yielding a 36% enhancement. The jet width and jet penetration distance from the outlet increase with an increase in methane flow rate and d*. When φ increases from 0.25 to 1.0, a higher φ increases the adiabatic combustion temperature and total heat release of the mixture, and also significantly improves the flame propagation speed. Faster flame propagation is beneficial for more complete combustion of the blends, thereby increasing the peak pressure inside the chamber. When the equivalence ratio is less than 1, the impact of the boundary layer blockage on jet performance becomes more significant as the equivalence ratio and d* drop. This is because the smaller d * increases the blockage caused by the boundary layer at the throat of the orifice, thereby increasing the viscous total pressure loss and reducing the effective mass flow rate. When the orifice loss is large, the efficiency of converting the increased chamber pressure into jet kinetic energy is also lower. When φ is small, the performance degradation caused by the decrease in d * becomes more pronounced. This is because lean combustion causes lower chamber pressure, combined with additional viscous losses from the small holes, further reducing the jet velocity.

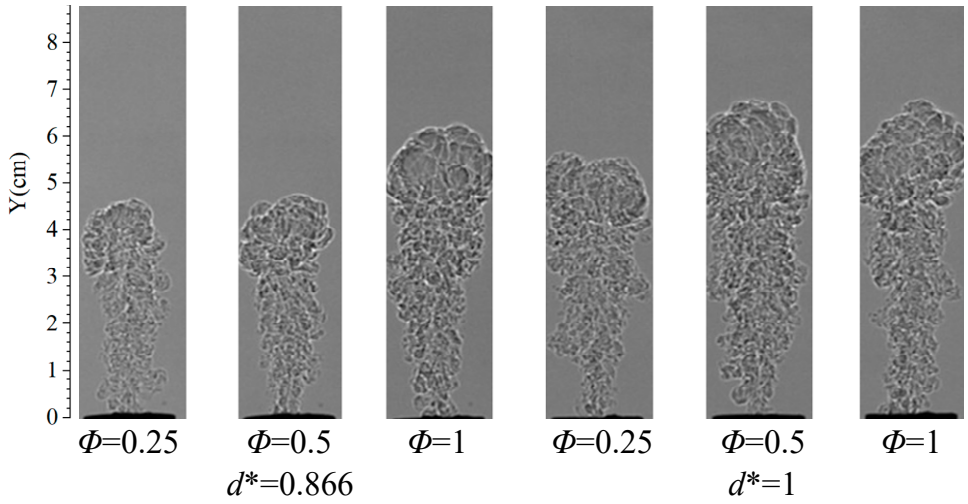


Figure 12. Shadowgraph images of V_c = 3140 mm^3 combustion-driven SparkJet actuator at different equivalence ratios and d* at 600 μs after discharge initiation.

3.2.3. The Influence of Different Cavity Volumes and Normalized Outlet Diameters on the Work Performance

Figures 14–19 depict the jet flow field structures of a combustion-driven SparkJet actuator with varying cavity volumes and normalized outlet diameters. From the figures, we can see that, for the normalized outlet diameter set at d* = 1 and with cavity volumes

V_c = 4710, 18,840, and 25,120 mm^3, a vortex ring structure and a precursor shock wave appear at the outlet of the combustion-driven SparkJet actuator at 40 μs. At 60 μs, the vortex ring structures and precursor shock waves only begin to appear for the combustion-driven SparkJet actuator with V_c = 3140 mm^3. At 80 μs, the combustion-driven SparkJet actuator with V_c = 4710 mm^3 presents a vortex string structure composed of two vortex rings in the jet flow field, but a continuous turbulent jet has not yet formed. The jet and precursor shock wave that appear at the outlet of the V_c = 18,840 and 25,120 mm^3 actuators are very weak. Moreover, the wave structure in the flow field is weaker than that in smaller-sized cavity actuators. At 600 μs, the actuator with V_c = 3140 mm^3 completes the high-temperature gas jet, while the completion times of the high-temperature gas jets for actuators with V_c = 4710, 18,840, and 25,120 mm^3 are approximately 1000, 1400, and 5000 μs, respectively. Meanwhile, the completion time of the high-temperature gas jet for the actuator with V_c = 4710 mm^3 is approximately 1400 μs when the normalized outlet diameter d* is 0.666. In addition, the jet intensity of the combustion-driven SparkJet actuator is higher than that of the plasma actuator, and the jet completion time is nearly the same as V_c = 4710 mm^3. Overall, the jet completion time of the actuator increases with an increase in cavity volume and decrease in normalized outlet diameter. Notably, the combustion-driven SparkJet actuator and the SparkJet actuator also have the same working frequency when the actuator volume is the same, indicating that the combustion process does not significantly extend the cycle time.

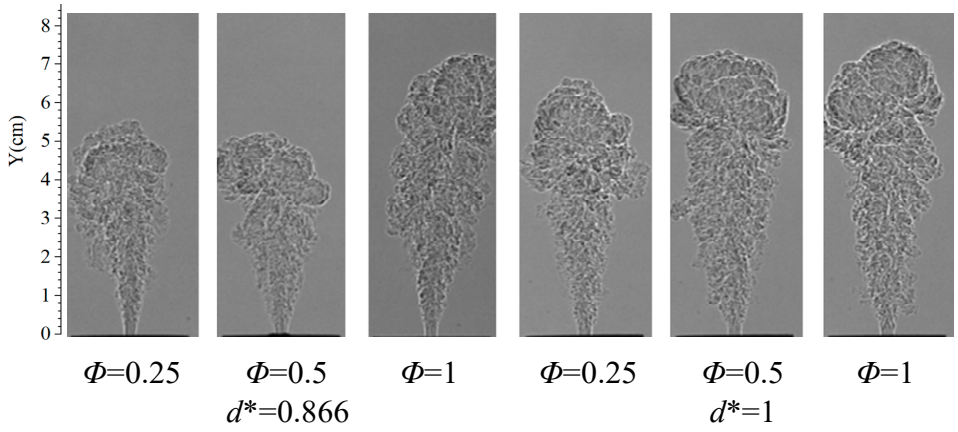


Figure 13. Shadowgraph images of V_c = 4710 mm^3 combustion-driven SparkJet actuator at different equivalence ratios and d* at 600 μs after discharge initiation.

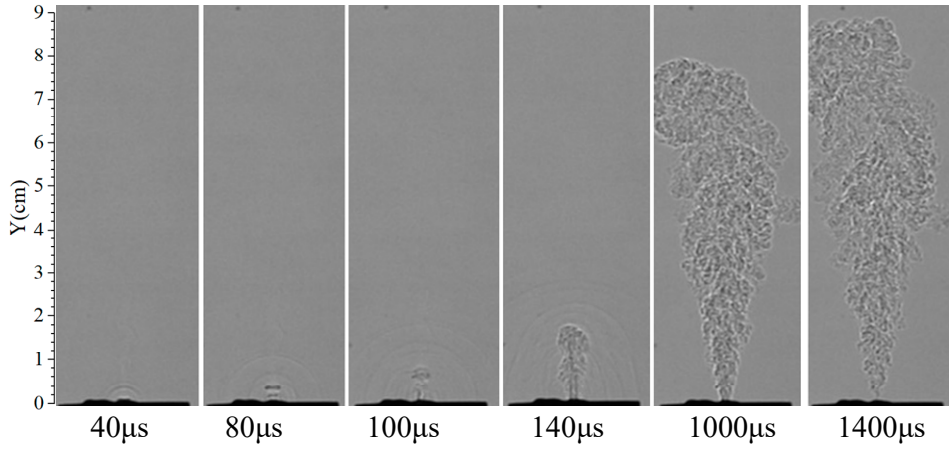


Figure 14. Shadowgraph images of combustion-driven SparkJet actuators at different times after discharge initiation when cavity volumes V_c and normalized outlet diameter d* equal 4710 mm^3 and 0.666, respectively.

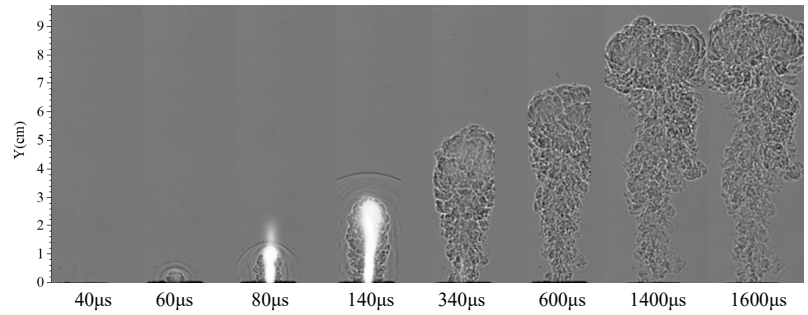


Figure 15. Shadowgraph images of combustion-driven SparkJet actuators at different times after discharge initiation when cavity volumes V_c and normalized outlet diameter d* equal 3140 mm^3 and 1, respectively.

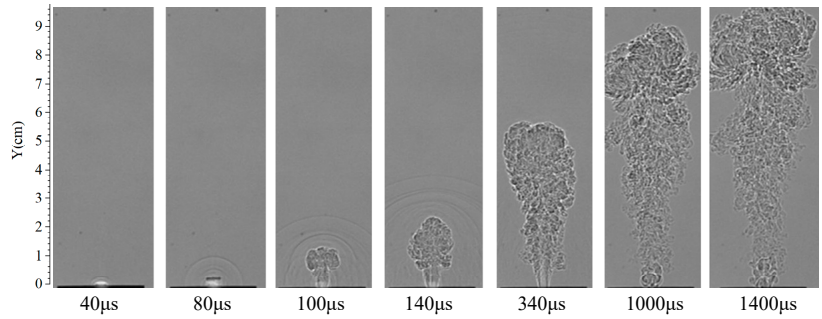


Figure 16. Shadowgraph images of combustion-driven SparkJet actuators at different times after discharge initiation when cavity volumes V_c and normalized outlet diameter d* equal 4710 mm^3 and 1, respectively.

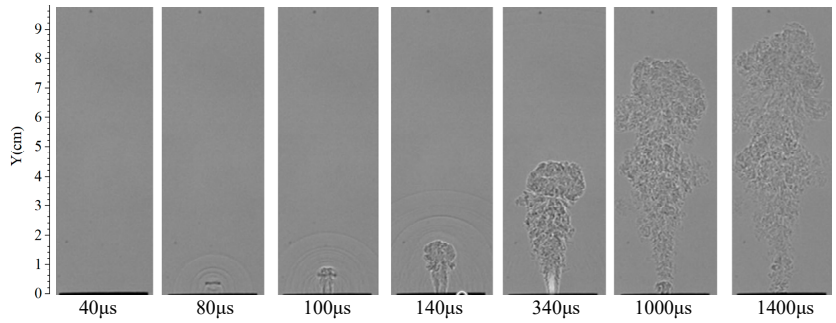


Figure 17. Shadowgraph images of SparkJet actuators at different times after discharge initiation when cavity volumes V_c and normalized outlet diameter d* equal 4710 mm^3 and 1, respectively.

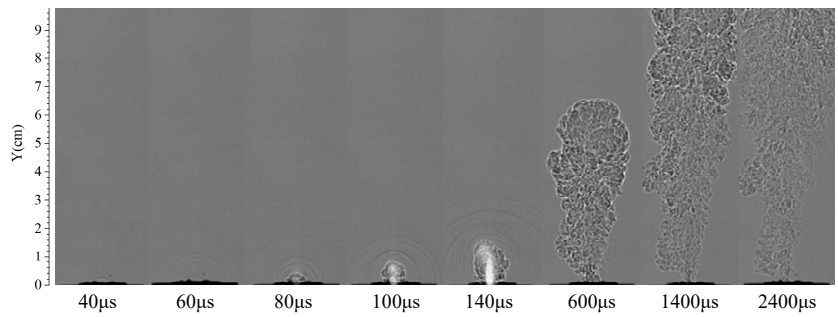


Figure 18. Shadowgraph images of combustion-driven SparkJet actuators at different times after discharge initiation when cavity volumes V_c and normalized outlet diameter d* equal 18,840 mm^3 and 1, respectively.

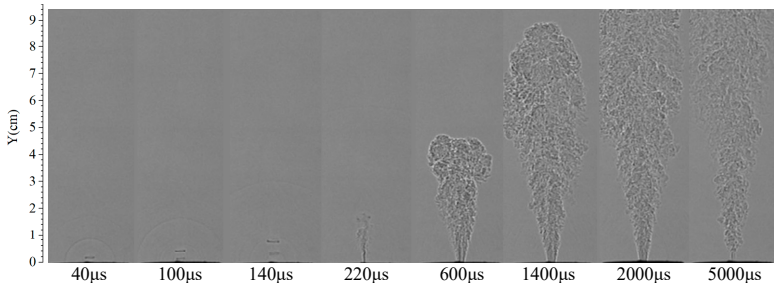


Figure 19. Shadowgraph images of combustion-driven SparkJet actuators at different times after discharge initiation when cavity volumes V_c and normalized outlet diameter d* equal 25,120 mm^3 and 1, respectively.

Figure 20 depicts the precursor shock wave measured in the jet flow field of the combustion-driven actuator, along with the jet penetration distance from the outlet, precursor shock wave, and jet velocities for a normalized outlet diameter set at 1 and different cavity volumes over 4 cycles. The distance from the precursor shock wave to the actuator outlet is shown to increase almost linearly with time, while the jet penetration distance from the outlet also increases but at a decreasing rate. The velocity of the precursor shock wave remains approximately 350 m/s, and the jet velocity of the combustion-driven actuator is higher than that of a plasma jet actuator under the same parameters. The maximum jet velocity of the actuator first increases as V_c increases from 3140 mm^3 to 4710 mm^3 and peaks at about 350 m/s, and then decreases as the volume further increases. The experimental results further confirm that the combustion performance has a significant impact on the optimal size.

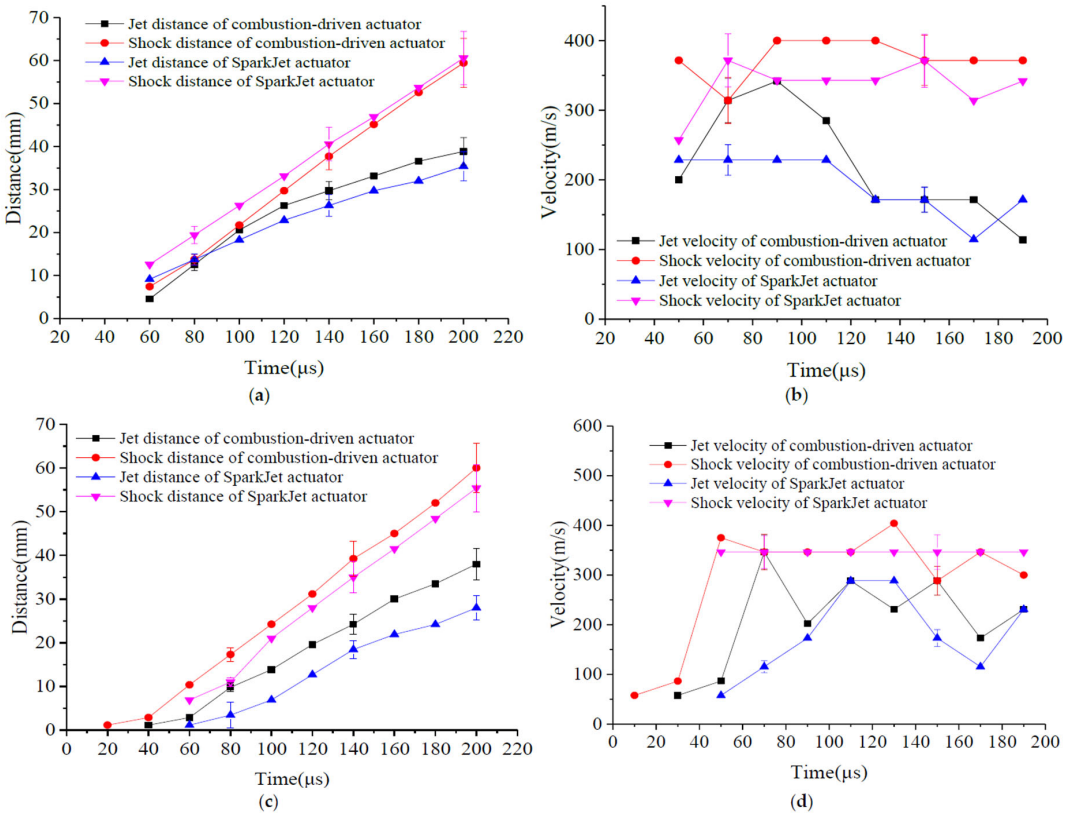


Figure 20. *Cont.*

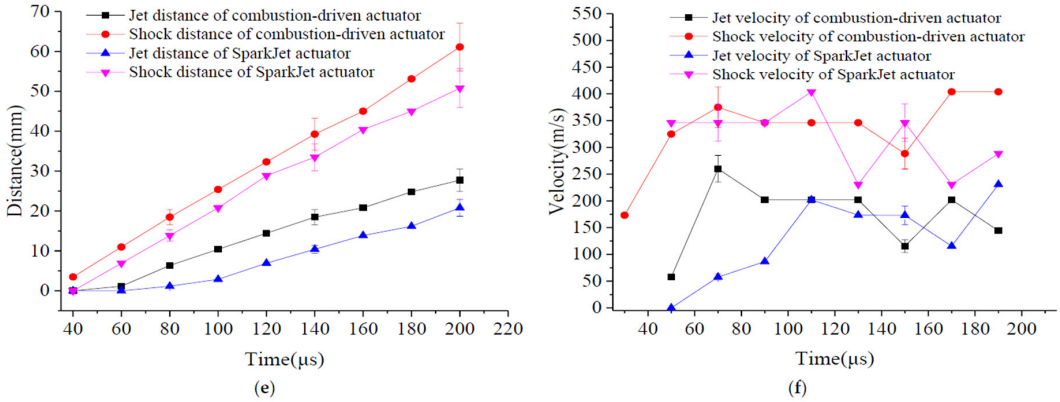


Figure 20. (**a**) Trajectory of the jet precursor shock and front jet when V_c equals 3140 mm^3; (**b**) variation in the maximum plasma synthetic jet velocity when V_c equals 3140 mm^3 for actuator; (**c**) trajectory of the jet precursor shock and front jet when V_c equals 4710 mm^3; (**d**) variation in the maximum plasma synthetic jet velocity when V_c equals 4710 mm^3 for actuator; (**e**) trajectory of the jet precursor shock and front jet when V_c equals 9231 mm^3; (**f**) variation in the maximum plasma synthetic jet velocity when V_c equals 9231 mm^3 for actuator.

However, there are several aspects worth further research to promote the practical application of such devices. First, this experiment was conducted at a discharge frequency of 1 Hz. The influence of discharge parameters on actuator performance can be studied in the future. Second, this work only studied a mixture of methane and air. The influence of other fuels such as hydrogen on the optimal geometric structure should be explored to obtain design principles. Third, research can be conducted on the improvement effect of combustion-driven plasma actuators on the working performance of transportation vehicles.

3.3. Optimization Design Suggestions for Combustion-Driven Spark Actuators

The experimental studies in this paper provide design references for combustion-driven spark actuators. Firstly, the volume of the cavity must be optimized rather than maximized. Different from plasma actuators, the jet velocity of plasma actuators decreases monotonically with increasing cavity volume, and combustion-driven actuators have an optimal cavity volume. For a methane–air mixture with a diameter of 1.0 and the current geometric structure, the optimal cavity volume is approximately 4710 mm^3. Secondly, increasing d* from 0.666 to 1 resulted in a 22% increase in jet penetration distance at V_c = 4710 mm^3. It is suggested that the optimal value of d * is larger than or equal to 1. In addition, the difference in jet penetration distance between d* = 0.666 and d* = 1 increased from approximately 0.8 mm at V_c = 3140 mm^3 to 2.2 mm at V_c = 9231 mm^3, indicating that the optimal value of d* will also change accordingly when the actuator size is adjusted. Thirdly, when $\varphi \leq 1.0$, the jet penetration distance increased monotonically with equivalence ratio because the equivalence ratio simultaneously increases the adiabatic flame temperature, total heat release, and laminar flame propagation speed. Therefore, it is recommended to operate on stoichiometric conditions to maximize jet momentum without affecting the operation of the actuators. Fourthly, the design optimization of combustion-driven spark injectors involves the coupling optimization of geometric parameters (V_c, d*), chemical parameters (fuel type, φ), and discharge parameters. This is fundamentally different from plasma actuators, whose optimization is essentially based on maximizing the discharge energy density. Fifth, the working frequency is not limited by the combustion process. The experimental results indicate that the jet completion time and saturation operating frequency of the combustion-driven actuator are comparable to those of a plasma actuator with the same cavity volume. This indicates that combustion will not reduce the operating frequency. Therefore, the

frequency optimization principle of combustion-driven spark actuators can refer to the plasma actuator.

4. Conclusions

This study experimentally investigated the static environmental performance of a methane combustion-driven SparkJet actuator. High-speed shadow imaging was used to characterize the spatiotemporal evolution of the jet flow field under different geometric and gas parameters of the actuator, and a direct comparison was made between the combustion-driven plasma actuator and the traditional plasma actuator. The main conclusions are as follows:

When the normalized outlet diameter of the actuator is 0.666–1, the distance from the combustion-driven plasma actuator front to the actuator outlet and the jet width increase with an increasing normalized outlet diameter. This is because the increase in normalized outlet diameter reduces the boundary layer blockage effect at the orifice throat, which reduces viscosity loss, thereby enhancing the mass flow rate and jet momentum.

When the normalized outlet diameter is 1, within the cavity volume range of 3140–25,120 mm^3, the jet width and jet penetration distance from the actuator outlet first increase and then decrease with an increase in cavity volume, peaking when the cavity volume is 4710 mm^3. This indicates that a larger volume results in a higher mixture mass inside the combustion-driven actuator and more released heat. On the other hand, the complete combustion of the mixture also takes longer, resulting in part of the mixture being discharged from the combustion chamber before complete combustion, which reduces the mixture combustion efficiency and the effective energy utilization rate in the combustion chamber. When the volume is the same, both the distance from the front face of the combustion-driven plasma actuator to the actuator outlet and the jet width are higher than those of the traditional plasma jet actuator. This is because the energy deposition mechanisms of the two types of actuators are different: plasma actuators rely only on limited electrical energy deposition, while combustion-driven actuators not only generate energy through discharge but also release chemical energy through the mixture combustion inside the chamber ignited by electrical energy. Therefore, combustion-driven actuators have an optimal volume parameter, and the design principles for combustion-driven plasma actuators are different from those for plasma actuators.

When the air flow rate is 800 mL/min and the methane flow rate ranges from 21 mL/min to 84 mL/min (equivalence ratio $\varphi \leq 1$), the distance from the combustion-driven actuator front to the actuator outlet and the jet width increase with an increasing methane flow rate. At an equivalence ratio less than 1, the combustion heat release increases with the methane flow rate, as do the jet velocity and jet width.

The distance from the precursor shock wave to the actuator outlet increases almost linearly with time, while the jet penetration distance from the outlet generally increases at a decreasing rate. The speed of the precursor shock wave remains at approximately 350 m/s. The jet speed driven by combustion in the actuator is higher than that of a traditional plasma jet actuator under the same parameters. The maximum jet speed of the actuator first increases due to enhanced combustion energy and then decreases due to the incomplete combustion occurring in oversized chambers.

These experimental results preliminarily characterize the working performance of methane combustion-driven SparkJet actuators under different sizes and inlet flow rates, providing effective references for the design and optimization of combustion-driven SparkJet actuators in the future. Firstly, the volume of the cavity must be optimized rather than maximized. For a methane–air mixture with an equivalence ratio of 1.0, the optimal cavity volume is approximately 4710 mm^3. Fuels with higher laminar flame speeds will permit

larger optimal volumes. The normalized outlet diameter should not be too small to minimize the viscosity loss caused by the boundary layer. The optimal value of d* will also change accordingly when the actuator size is adjusted. The equivalence ratio should be as close as possible to the stoichiometric conditions to maximize the volumetric heat release rate, flame propagation speed, and jet velocity. The design optimization of combustion-driven actuators is essentially multiparameter, involving the coupling optimization of geometric shape, fuel parameters, and discharge conditions. This is different from the design of PSJ actuators, which are mainly dominated by discharge energy density. The combustion process does not significantly extend the actuator cycle time, indicating that working frequency optimization can follow the principles for plasma actuators.

Author Contributions: Conceptualization, H.C.; Methodology, H.C.; Validation, H.C.; Writing—Original Draft, H.C.; Writing—Review and Editing, H.C.; Supervision, H.Z., G.J. and J.Z. All authors have read and agreed to the published version of the manuscript.

Funding: This research received no external funding.

Institutional Review Board Statement: Not applicable.

Informed Consent Statement: Not applicable.

Data Availability Statement: Data are contained within the article.

Acknowledgments: We are grateful to the National University of Defense Technology for assistance with the experiments.

Conflicts of Interest: The authors declare no conflicts of interest.

References

1. Popov, N.A. Kinetics of plasma-assisted combustion: Effect of non-equilibrium excitation on the ignition and oxidation of combustible mixtures. *Plasma Sources Sci. Technol.* **2016**, *25*, 043002. [CrossRef]
2. Frischmuth, T.; Schneider, M.; Maurer, D.; Grille, T.; Schmid, U. Inductively-coupled plasma-enhanced chemical vapour deposition of hydrogenated amorphous silicon carbide thin films for MEMS. *Sens. Actuators A Phys.* **2016**, *247*, 647–655. [CrossRef]
3. Zhang, X.; Li, H.X.; Huang, Y.; Wang, W.B. Wing Flow Separation Control Using Asymmetrical and Symmetrical Plasma Actuator. *J. Aircr.* **2016**, *54*, 301–309.
4. Kelley, C.L.; Corke, T.C.; Thomas, F.O.; Patel, M.; Cain, A.B. Design and Scaling of Plasma Streamwise Vortex Generators for Flow Separation Control. *AIAA J.* **2016**, *54*, 3397–3408. [CrossRef]
5. Wang, L.; Luo, Z.; Xia, Z.; Liu, B.; Deng, X. Review of actuators for high speed active flow control. *Sci. China* (*Technol. Sci.*) **2012**, *55*, 2225–2240. [CrossRef]
6. Grossman, K.R.; Cybyk, B.Z.; VanWie, D.M. SparkJet Actuators for Flow Control. In Proceedings of the 41st Aerospace Sciences Meeting and Exhibit, Reno, NV, USA, 6–9 January 2003; AIAA Paper.
7. Narayanaswamy, V.; Raja, L.L.; Clemens, N.T. Characterization of a High-frequency Pulsed-plasma Jet Actuator for Su-personic Flow Control. *AIAA J.* **2010**, *48*, 297–305. [CrossRef]
8. Huang, H.X.; Tan, H.J.; Sun, S.; Zhang, Y.C.; Cheng, L. Transient Interaction Between Plasma Jet and Supersonic Compression Ramp Blow. *Phys. Fluids* **2018**, *30*, 041703. [CrossRef]
9. Li, J.F.; Zhang, X.B. Active Flow Control for Surpersonic Aircraft: A Novel Hybird Synthetic Jet Actuator. *Sens. Actuators A Phys.* **2020**, *302*, 111770. [CrossRef]
10. Liu, R.B.; Wang, M.M.; Hao, M.; Lin, Q.; Wang, X.G. Experimental research on air supplementing type plasma synthetic jet generator. *Acta Aeronaut. Astronaut. Sin.* **2016**, *37*, 1713–1721.
11. Tang, M.X.; Wu, Y.; Wang, H.Y.; Jin, D.; Guo, S.G.; Gan, T. Effects of Capacitance on a Plasma Synthetic Jet Actuator with a Conical Cavity. *Sens. Actuators A Phys.* **2018**, *276*, 284–295. [CrossRef]
12. Zhang, Z.B.; Wu, Y.; Sun, Z.Z.; Song, H.M.; Jia, M.; Zong, H.H.; Li, Y.H. Experimental Research on Multichannel Discharge Circuit and Multi-Electrode Plasma Synthetic Jet Actuator. *J. Phys. D Appl. Phys.* **2017**, *50*, 165205. [CrossRef]
13. Jin, D.; Li, Y.H.; Jia, M.; Song, H.H.; Cui, W.; Sun, Q.; Li, F.Y. Experimental Characterization of the Plasma Synthetic Jet Actuator. *Plasma Sci. Technol.* **2013**, *15*, 1034–1040. [CrossRef]
14. Kim, H.J.; Shin, J.Y.; Chae, J.; Ahn, S.; Kim, K.H. Numerical investigation on jet characteristics and performance of SparkJet actuator based on pressure wave behavior inside a cavity. *AIP Adv.* **2020**, *10*, 035024. [CrossRef]

15. Zheng, B.; Zhang, Q.; Zhao, T.; Song, G.; Chen, Q. Experimental and numerical investigation of a self-supplementing dual-cavity plasma synthetic jet actuator. *Plasma Sci. Technol.* **2023**, *25*, 025503. [CrossRef]
16. Wu, S.; Liu, X.; Huang, G.; Liu, C.; Bian, W.; Zhang, C. Influence of high-voltage pulse parameters on the propagation of a plasma synthetic jet. *Plasma Sci. Technol.* **2019**, *21*, 60–68. [CrossRef]
17. Zhang, W.; Geng, X.; Shi, Z.; Jin, S. Study on Inner Characteristics of Plasma Synthetic Jet Actuator and Geometric Effects. *Aerosp. Sci. Technol.* **2020**, *105*, 106044. [CrossRef]
18. Haohua, Z.; Kotsonis, M. Effect of slotted exit orifice on performance of plasma synthetic jet actuator. *Exp. Fluids* **2017**, *58*, 17. [CrossRef]
19. Yue, L.; Wang, Y.F.; Zhang, Y.W.; Zhao, X. Effect of Plasma Actuator on Flow Field. *Acta Phys. Pol. A* **2022**, *141*, 74. [CrossRef]
20. Nguyen, H.H.; Shin, J. Jet Characteristics of Pulsed Arc SparkJet Actuator and Performance Improvement with Dual-Spark Pulses. *Int. J. Aeronaut. Space Sci.* **2023**, *24*, 411–418. [CrossRef]
21. Liu, R.; Xue, S.; Wei, W.; Lin, Q.; Tang, K. Internal Characteristics of Air-Supplied Plasma Synthetic Jet Actuator. *Aerospace* **2023**, *10*, 223. [CrossRef]
22. Cheng, L.; Sun, X.L.; Ma, S. Three-dimensional Flow Field Characteristics of a Normal Slot Plasma Synthetic Jet Actuator. *J. Appl. Fluid Mech.* **2024**, *17*, 1457–1469. [CrossRef]
23. Zhang, X.; Dong, H.; Cao, X.; Zhou, Y.; Xie, W.; Song, W.; Wang, Y. Investigation into Shock Control and Drag Reduction Characteristics of Opposing Plasma Synthetic Jet in Mach 8 Flow. *Aerospace* **2025**, *12*, 17. [CrossRef]
24. Liu, R.; Xue, S.; Lin, R.; Chen, Y.; Lin, Q. Plasma synthetic jet actuator array driven by a programmable triggered Marx high-voltage generator. *Aerosp. Sci. Technol.* **2024**, *145*, 108876. [CrossRef]
25. Shin, J.Y.; Kim, K.H. Numerical study and modal analysis of electrode position and energy deposition amount effects on SparkJet actuator performance. *Phys. Fluids* **2025**, *37*, 016114. [CrossRef]
26. Kong, Y.; Wang, C.; Zong, H.; Wu, Y.; Liang, H.; Tang, M.; Qu, Y. Supersonic Cavity Flow Control Using Plasma Synthetic Jet Actuators. *AIAA J.* **2025**, *63*, 1732–1742. [CrossRef]
27. Li, L.; Yuan, Z.; Xiang, Y.; Fan, A. Numerical investigation on mixing performance and diffusion combustion characteristics of H2 and air in planar micro-combustor. *Int. J. Hydrogen Energy* **2018**, *43*, 12491–12498. [CrossRef]
28. Chen, H.; Liu, W.Q. Numerical Investigation of the Combustion in an Improved Micro combustion Chamber with Rib. *J. Chem.* **2019**, *2019*, 8354541. [CrossRef]
29. Chen, H.; Liu, W.Q. Numerical study of effect of front cavity on hydrogen/air premixed combustion in a micro-combustion chamber. *J. Cent. South Univ.* **2019**, *26*, 2259–2271. [CrossRef]
30. Hua, J.; Meng, W.; Kumar, K. Numerical simulation of the combustion of hydrogen–air mixture in micro-scaled chambers. Part I: Fundamental study. *Chem. Eng. Sci.* **2005**, *60*, 3497–3506. [CrossRef]
31. Crittenden, T.; Glezer, A.; Funk, R.; Parekh, D. Combustion-Driven Jet Actuators for Flow Control. In Proceedings of the 15th AIAA Computational Fluid Dynamics Conference, Anaheim, CA, USA, 11–14 June 2001.
32. Jee, S.; Bowles, P.O.; Matalanis, C.G.; Min, B.Y.; Wake, B.E.; Crittenden, T.; Glezer, A. Computations of Combustion-Powered Actuation for Dynamic Stall Suppression. In Proceedings of the American Helicopter Society (AHS) Annual Forum, West Palm Beach, FL, USA, 15 July 2016.
33. Srinivasan, S.; Girgis, B.; Menon, S. Large-Eddy Simulation of a Combustion Powered Actuator. In Proceedings of the 44th AIAA/ASME/SAE/ASEE Joint Propulsion Conference & Exhibit, Hartford, CT, USA, 21–23 July 2008; AIAA Paper.
34. Rajendar, A.; Crittenden, T.; Glezer, A. Effect of Inlet Flow Configuration on Combustion Powered Actuators. In Proceedings of the 48th AIAA Aerospace Sciences Meeting Including the New Horizons Forum and Aerospace Exposition, Orlando, FL, USA, 4–7 January 2010; AIAA Paper.
35. Crittenden, T.M.; Warta, B.J.; Glezer, A. Characterization of Combustion Powered Actuators for Flow Control. In Proceedings of the 3rd AIAA Flow Control Conference, San Francisco, CA, USA, 5–8 June 2006.
36. Chen, H.; Zhou, Y.; Luo, Z.; Cheng, P. Numerical Investigation of Effect of Structural Parameters on the Performance of a Combustion-Driven Sparkjet Actuator. *Actuators* **2023**, *12*, 250. [CrossRef]
37. Chen, H.; Zuo, H.; Jia, G. Numerical Simulation of the Performance of a Combustion-Driven SparkJet Actuator a with Laval Outlet Configuration. *Actuators* **2025**, *14*, 145. [CrossRef]
38. Reedy, T.M.; Kale, N.V.; Dutton, J.C.; Elliott, G.S. Experimental Characterization of a Pulsed Plasma Jet[R]. *AIAA Pap.* **2013**, *51*, 2027–2031. [CrossRef]
39. Ko, H.S.; Haack, S.J.; Land, H.B.; Cybyk, B.; Katz, J.; Kim, H.J. Analysis of Flow Distribution from High-Speed Flow Actuator Using Particle Image Velocimetry and Digital Speckle Tomography. *Flow Meas. Instrum.* **2010**, *21*, 443–453. [CrossRef]
40. Belinger, A.; Hardy, P.; Gherardi, N.; Naude, N.; Cambronne, J.P.; Caruana, D. Influence of the Spark Discharge Size on a Plasma Synthetic Jet Actuator. *IEEE Trans. Plasma Sci.* **2011**, *39*, 2334–2335. [CrossRef]
41. Shin, J. Characteristics of High Speed Electro-thermal Jet Activated by Pulsed DC Discharge. *Chin. J. Aeronaut.* **2010**, *23*, 518–522. [CrossRef]

42. Belinger, A.; Hardy, P.; Barricau, P.; Cambronne, J.P.; Caruana, D. Influence of the Energy Dissipation Rate in the Discharge of A Plasma Synthetic Jet Actuator. *J. Phys. D Appl. Phys.* **2011**, *44*, 365201. [CrossRef]
43. Emerick, T.M., II; Ali, M.Y.; Foster, C.H.; Alvi, F.S.; Popkin, S.H.; Cybyk, B.Z. SparkJet Actuator Characterization in Super-sonic Crossflow. In Proceedings of the 6th AIAA Flow Control Conference, New Orleans, LA, USA, 25 June 2012–28 June 2012.

Disclaimer/Publisher's Note: The statements, opinions and data contained in all publications are solely those of the individual author(s) and contributor(s) and not of MDPI and/or the editor(s). MDPI and/or the editor(s) disclaim responsibility for any injury to people or property resulting from any ideas, methods, instructions or products referred to in the content.